



PAPER

OPEN ACCESS

RECEIVED

21 December 2023

REVISED

18 April 2024

ACCEPTED FOR PUBLICATION

28 May 2024

PUBLISHED

20 June 2024

Original Content from
this work may be used
under the terms of the
[Creative Commons
Attribution 4.0 licence](#).

Any further distribution
of this work must
maintain attribution to
the author(s) and the title
of the work, journal
citation and DOI.



Topology of surface electromyogram signals: hand gesture decoding on Riemannian manifolds

Harshavardhana T Gowda¹ and Lee M Miller^{2,*} ¹ Department of Electrical and Computer Engineering, University of California, Davis, CA 95616, United States of America² Center for Mind and Brain; Department of Neurobiology, Physiology, and Behavior; Department of Otolaryngology-Head and Neck Surgery, University of California, Davis, CA 95616, United States of America

* Author to whom any correspondence should be addressed.

E-mail: leemiller@ucdavis.edu and tgharshavardhana@gmail.com**Keywords:** EMG, sEMG, decoding, classification, manifold, Riemannian, hand gestures

Abstract

Objective. Decoding gestures from the upper limb using noninvasive surface electromyogram (sEMG) signals is of keen interest for the rehabilitation of amputees, artificial supernumerary limb augmentation, gestural control of computers, and virtual/augmented realities. We show that sEMG signals recorded across an array of sensor electrodes in multiple spatial locations around the forearm evince a rich geometric pattern of global motor unit (MU) activity that can be leveraged to distinguish different hand gestures. **Approach.** We demonstrate a simple technique to analyze spatial patterns of muscle MU activity within a temporal window and show that distinct gestures can be classified in both supervised and unsupervised manners. Specifically, we construct symmetric positive definite covariance matrices to represent the spatial distribution of MU activity in a time window of interest, calculated as pairwise covariance of electrical signals measured across different electrodes. **Main results.** This allows us to understand and manipulate multivariate sEMG timeseries on a more natural subspace—the Riemannian manifold. Furthermore, it directly addresses signal variability across individuals and sessions, which remains a major challenge in the field. sEMG signals measured at a single electrode lack contextual information such as how various anatomical and physiological factors influence the signals and how their combined effect alters the evident interaction among neighboring muscles. **Significance.** As we show here, analyzing spatial patterns using covariance matrices on Riemannian manifolds allows us to robustly model complex interactions across spatially distributed MUs and provides a flexible and transparent framework to quantify differences in sEMG signals across individuals. The proposed method is novel in the study of sEMG signals and its performance exceeds the current benchmarks while being computationally efficient.

1. Introduction

sEMG signals are recorded non-invasively by placing sensors on the skin surface and measuring electrical signals arising from motor unit (MU) activation. Global characteristics of the sEMG signal such as its amplitude and power spectrum depend on numerous idiosyncratic factors: anatomical characteristics including thickness of the subcutaneous tissue, distribution and size of MU territories, and spread of endplates and tendon junctions within the MU; physiological factors such as distribution of conduction velocities of the fibers within the MUs, shape of

intracellular action potentials [5], and muscle fatigue [4]; and circumstantial factors such as the precise electrode placement [9, 12]. The combined effect of these factors is further complicated by the interactions of signals originating from multiple, neighboring muscles. Consequently, signals from individual sEMG electrodes tend to be highly confounded and opaque, thereby limiting their practical use. We show that covariance matrices constructed using pairwise covariance of electrical signals measured across different electrodes capture the combined effect of various physiological and anatomical factors and provide a framework to quantify the differences in sEMG

signals across individuals. Moreover, the spatial signal patterns captured by covariance matrices showcase rich geometric patterns that can be used to distinguish distinct hand gestures.

Existing methods use constructed features such as signal root-mean-square, time domain statistics as described by Hudgins *et al* [8], histograms [28], marginalized discrete wavelet transform [16], or the normalized combination of all of the above. These features are often evaluated with classifiers such as linear discriminant analysis (LDA), support vector machines, k -nearest neighbors (k -NN), and random forests. Additionally, some works use deep learning models such as convolutional neural networks (CNN) [6, 11, 22, 25], recurrent neural networks (RNN) [19, 23], transformer-based networks [18, 20], and networks constructed by combining RNN and CNN [7, 21]. Xiong *et al* [26] analyze sEMG signals using symmetric positive definite (SPD) covariance matrices; however, by mapping the learned features on the manifold onto a tangent plane and by decoding them in the Euclidean space, this approach does not leverage the advantages of the natural geometrical structure of the data. All of the above methods fail to account for strong spatial correlations in the muscle contraction patterns. Additionally, these approaches may have a large number of training parameters, in the range of tens of thousands, and tend to require complex transfer learning paradigms and retraining while deploying across individuals. None of the established techniques easily adapt to signal changes due to factors such as muscle fatigue and deviations in sensor positions.

We demonstrate that analysis of sEMG signals on a Riemannian manifold is more comprehensive and naturally suited for the data structure than the usual analysis in Euclidean space. SPD covariance matrices constructed from the multivariate sEMG timeseries lie on a cone manifold equipped with a Riemannian metric. For computational efficiency and numerical stability, we study the SPD matrices via Cholesky decomposition in the Cholesky space [15], the collection of lower triangular matrices whose diagonal elements are all positive. We demonstrate that covariance matrices from different individuals lie in different neighborhoods of the manifold space owing to the combined influence of an individual's anatomical and physiological factors on the sEMG signals and that the difference in sEMG signals among individuals can be quantified using the geodesic distance (length of the shortest curve between two points on a surface) between corresponding covariance matrices. We present two supervised learning algorithms (manifold minimum distance to mean (MDM) and manifold support vector machine (SVM)) and one unsupervised learning algorithm (manifold k -medoids clustering) to classify hand gestures on the Riemannian manifold.

2. Methods

We describe below the principles of using SPD covariance matrices, the means of operating on the Riemannian Manifold, and the distance metrics with which we characterize variability, e.g. across individual subjects and distinct gestures.

2.1. Definitions

For a square matrix X , whose dimension is c , $X(i, j)$ denotes its element in the i th row and j th column. $[X]$ denotes a $c \times c$ matrix whose (i, j) element is X_{ij} if $i > j$ and is zero otherwise. $\mathbb{D}(X)$ denotes a $c \times c$ diagonal matrix whose (i, i) element is X_{ii} . For two square matrices X and Y , Frobenius inner product $\langle X, Y \rangle_F = \sum_{ij} X_{ij} Y_{ij}$ and the induced Frobenius norm is $\|X\| = \langle X, X \rangle_F^{1/2}$. For X , a lower triangular matrix $X_{\frac{1}{2}}$ is defined as $X_{\frac{1}{2}} = [X] + \mathbb{D}(X)/2$. The matrix exponential map of a real matrix is defined by $\exp(X) = \sum_{k=0}^{\infty} \frac{X^k}{k!}$ and its inverse, the matrix logarithm, whenever it exists and is real, is denoted by $\log(X)$. It is noted that the matrix exponential and logarithm of a diagonal matrix is also a diagonal matrix. Mathematical formulation and notations used here are borrowed from Lin [15].

2.2. Operating on the manifold of SPD matrices

SPD matrices of dimension c , denoted by \mathcal{S}_c^+ , is a convex smooth submanifold of the space \mathcal{S}_c of symmetric matrices with the Euclidean space $\mathbb{R}^{c(c+1)/2}$. For a matrix $P \in \mathcal{S}_c^+$, Cholesky decomposition expresses P as a product of lower triangular matrix L and its transpose; that is, $P = LL^T$. If the diagonal elements of L are restricted to be positive, Cholesky decomposition is unique [15]. Lower triangular matrices of dimension c whose diagonal elements are all positive, denoted by \mathcal{L}_c^+ , is a smooth submanifold of the space \mathcal{L}_c of lower triangular matrices with the Euclidean space $\mathbb{R}^{c(c+1)/2}$. Cholesky decomposition denoted by $\mathcal{L} : \mathcal{S}_c^+ \rightarrow \mathcal{L}_c^+$ is bijective, that is, there is a one-to-one correspondence between SPD matrices and lower triangular matrices whose diagonal elements are all positive [15]. The inverse map is denoted by $\mathcal{S} : \mathcal{L}_c^+ \rightarrow \mathcal{S}_c^+$. \mathcal{L} and its inverse \mathcal{S} are diffeomorphisms, that is, differentiable map \mathcal{L} is a bijection and its inverse \mathcal{S} is differentiable as well. Space \mathcal{S}_c^+ is the Riemannian space and the space \mathcal{L}_c^+ is the Cholesky space.

2.3. Riemannian metrics

Tangent space at a given matrix in \mathcal{S}_c^+ is identified with \mathcal{S}_c . Tangent space at a given matrix in \mathcal{L}_c^+ is identified with \mathcal{L}_c . For $L \in \mathcal{L}_c^+$ and X, Y in the tangent space at L denoted by $T_L \mathcal{L}_c^+$ (identified with \mathcal{L}_c), Riemannian metric \tilde{g} for tangent space is given by

$$\tilde{g}_L(X, Y) = \sum_{i>j} X_{ij}Y_{ij} + \sum_{j=1}^c X_{jj}Y_{jj}L_{jj}^{-2}. \quad (1)$$

Riemannian metric g for $P \in \mathcal{S}_c^+$ and $W, V \in \mathcal{T}_P\mathcal{S}_c^+$ (identified with \mathcal{S}_c) is given by

$$g_P(W, V) = \tilde{g}_L \left(L(L^{-1}WL^{-T})_{\frac{1}{2}}, L(L^{-1}VL^{-T})_{\frac{1}{2}} \right), \quad (2)$$

where $L = \mathcal{L}(P)$. The map \mathcal{L} is an isometry between $(\mathcal{L}_c^+, \tilde{g})$ and (\mathcal{S}_c^+, g) [15]. A Riemannian isometry provides correspondence of Riemannian properties and objects between two Riemannian manifolds. This enables us to study the properties of (\mathcal{S}_c^+, g) via the manifold $(\mathcal{L}_c^+, \tilde{g})$ and the isometry \mathcal{L} . The metrics presented here are computationally efficient and numerically stable compared to affine-invariant and Log-Euclidean metrics (directly operating with SPD matrices using affine-invariant Riemannian metric involves computing matrix logarithm and exponential which involve evaluating a series of infinite terms [1]). Specifically, under this construction, Fréchet mean and parallel transport are given in a closed form and we can construct a positive definite kernel for SVM (which is not possible with the affine-invariant metric [10]).

2.3.1. Geodesic distance metric

For any two points L, K in \mathcal{L}_c^+ , we have a unique geodesic curve (shortest path between two points) connecting L and K . The arc length of the geodesic curve, that is, the geodesic distance in \mathcal{L}_c^+ between L and K is given by

$$d_{\mathcal{L}_c^+}(L, K) = \left\{ \left(\|L\| - \|K\| \right)^2 + \left(\log \mathbb{D}(L) - \log \mathbb{D}(K) \right)^2 \right\}^{1/2}. \quad (3)$$

2.3.2. Average of finite SPD matrices

For $L_1, L_2, \dots, L_n \in \mathcal{L}_c^+$, the Fréchet average is

$$\mathbb{E}_n(L_1, L_2, \dots, L_n) = \frac{1}{n} \sum_{i=1}^n [L_i] + \exp \left(\frac{1}{n} \sum_{i=1}^n \log \mathbb{D}(L_i) \right). \quad (4)$$

2.4. MDM algorithm

Given M classification classes and N training samples, SPD matrices in the training set $\{\mathcal{S}_n^m\}$, where $n \in \{1, 2, \dots, N\}$ and $m \in \{1, 2, \dots, M\}$ are used to construct centroids for each of the M classes such that the centroid of class m is,

$$\mathcal{C}^m = \mathbb{E}(\{\mathcal{L}(\mathcal{S}_n^m)\}), \quad (5)$$

where the Fréchet mean is calculated according to equation (4). Given a test dataset of SPD matrices

$\{\mathcal{T}\}$, $T \in \mathcal{T}$ is assigned to that class whose centroid is nearest to $\mathcal{L}(T)$. That is, the class of T is

$$\arg \min_m d_{\mathcal{L}_c^+}(\mathcal{L}(T), \mathcal{C}^m). \quad (6)$$

2.5. k -Medoids algorithm

We implement the classic k -medoids algorithm using partitioning around medoids heuristic by replacing the Euclidean distance with the distance in equation (3).

2.6. SVM

For training the SVM, we use a kernel $\mathcal{K} : \mathcal{L}_c^+ \times \mathcal{L}_c^+ \rightarrow \mathbb{R}$, such that

$$\mathcal{K} = \exp \left(-\gamma d_{\mathcal{L}_c^+}^2(L_1, L_2) \right), \quad (7)$$

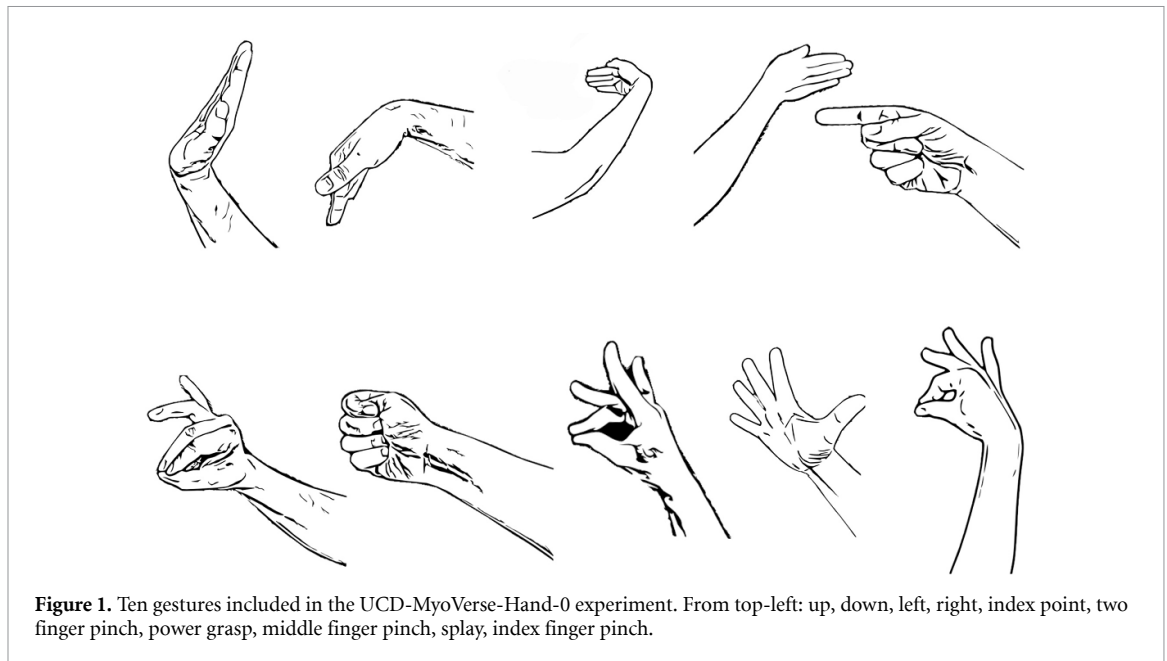
where $L_1, L_2 \in \mathcal{L}_c^+$ and $\gamma > 0$. In appendix A, following the arguments in Jayasumana *et al* [10], we prove that the kernel in equation (7) is a valid kernel.

3. Datasets

We use three data sets in this study. The first (Ninapro) is publicly available from Atzori *et al* [2], the second (high density sEMG signals) is publicly available from Malešević *et al* [17], and the third (UCD-MyoVerse-Hand-0) was collected and curated by us at the University of California, Davis.

3.1. Dataset 1 - Ninapro

We choose the widely used *Ninapro* (Non-Invasive Adaptive Prosthetics) *Database 2-Exercise 1* [2] to test our algorithms and to compare them against the existing benchmarks. The dataset consists of sEMG signals obtained from forty intact subjects using twelve electrodes. Eight electrodes were placed equally spaced around the forearm at the height of the radio-humeral joint; two electrodes were placed on the main activity spots of the flexor digitorum superficialis and of the extensor digitorum superficialis. Subjects performed seventeen different gestures, each repeated six times. The seventeen gestures are: thumb up, extension of index and middle—flexion of the others, flexion of ring and little finger—extension of the others, thumb opposing base of little finger, abduction of all fingers, fingers flexed together in fist, pointing index, adduction of extended fingers, wrist supination (axis: middle finger), wrist pronation (axis: middle finger), wrist supination (axis: little finger), wrist pronation (axis: little finger), wrist flexion, wrist extension, wrist radial deviation, wrist ulnar deviation, and wrist extension with closed hand. See Atzori *et al* [2] for further details on data acquisition and processing.



3.2. Dataset 2 - high density sEMG signals from Malešević *et al* [17]

The dataset consists of sEMG signals obtained from nineteen intact subjects using 128 electrodes recorded at the level of the forearm. (The experiment included twenty intact subjects, however the data corresponding to *Subject 5* is corrupted.) Subjects performed 65 unique gestures that are combinations of 16 basic single degree of freedom movements. Each gesture was repeated five times. See Malešević *et al* [17] for further details on data acquisition and processing.

3.3. Dataset 3 - UCD-MyoVerse-Hand-0

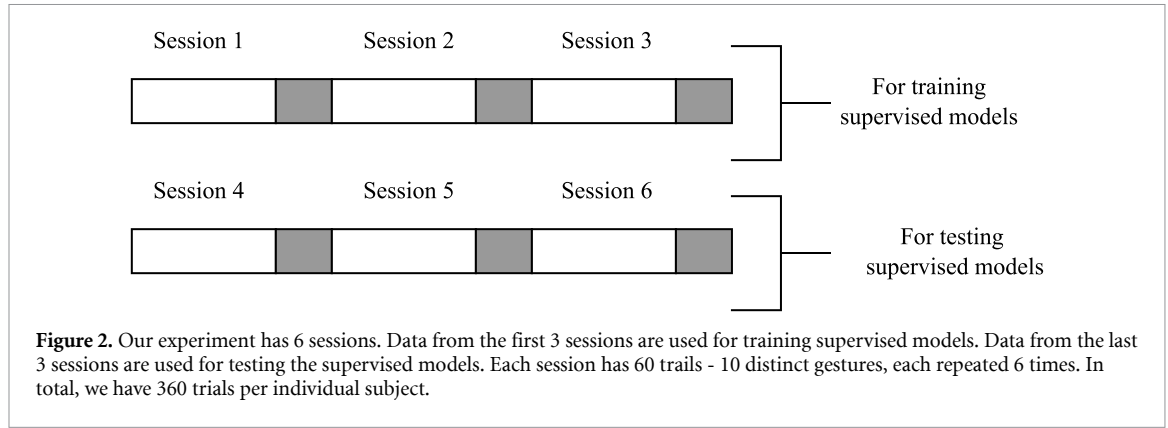
A total of thirty subjects (age range: 18–76 years) participated in our study. Forearm sEMG was collected from intact subjects using twelve electrodes. Eight electrodes were placed equally spaced around the main belly of the forearm muscles below the elbow at approximately 1/3 the distance from elbow to wrist. Four electrodes were placed equally spaced around the wrist joint. Each subject performed ten different hand gestures, with each gesture performed thirty-six times. The ten gestures are: wrist movement in four cardinal directions (up, down, left, and right), three pinches (index finger pinch, middle finger pinch, two-finger pinch), splay, power grasp, and pointing index (figure 1). The 10 gestures were chosen to reflect the commonly used gestures for interacting with computers. Hand gestures in cardinal directions can be used to move the screen up, down, left, and right. The pinches can be used for zoom-in, zoom-out, and selections.

3.3.1. Data acquisition protocol

For *Dataset 3*, we use Delsys double differential sEMG electrodes (Delsys, Inc) and NI USB-6210 multifunction I/O (National Instruments

Corporation — 16-inputs, 16-bit, 250kS/s) data acquisition system for acquiring sEMG data at a rate of 2000 *Hertz*. Delsys electrodes transmitted the acquired data via a wireless network to the base station. Data from the base station was relayed to the computer via a USB connection through the NI USB-6210 data acquisition system. A graphical user interface (GUI) was designed to display hand gestures on a screen. Subjects performed the displayed gesture with their dominant hand while comfortably seated in a chair with the forearm resting on an elevated platform on the table (subjects were allowed to choose a resting position that they were most comfortable with. They were also allowed to change the resting position throughout the experiment). Each gesture lasted for 2 s followed by a resting period of 2 s. (The gesture was displayed on the screen for a period of 2 s followed by a blank screen for a period of 2 s; subjects were instructed to perform the gesture for the duration the image was present on the screen and rest during the blank screen.) The experiment was divided into six sessions (figure 2). Each session consisted of sixty trials: six repetitions for each of the ten gestures. The order of gestures within a session was pseudorandomly generated. This was done to assess how variations in making gestures affect the decoding accuracy (if all 6 repetitions for a gesture occurred sequentially, it would encourage repetitive and almost unconscious and extremely consistent movements). In total, each subject completed 360 trials.

We used ZeroMQ sockets (<https://zeromq.org/socket-api/>) and Lab Streaming Layer (<https://github.com/scn/labstreaminglayer>) in Python to time sync GUI instructions with data streamed from the Delsys system. Data streams were synced to the master clock on the computer that received both sEMG data and



event markers from the GUI. We observed a maximum clock drift of around 50 ms.

4. Results

4.1. Dataset 1

4.1.1. Preprocessing

In *Dataset 1*, sEMG data was collected at a frequency of 2000 Hz using 12 electrodes. Each gesture was 5 s long followed by a 3 s resting position. We use *Database B - Exercise 1* with 17 hand gestures. For a detailed description, refer to Atzori *et al* [2]. For each gesture, sEMG data is a matrix X which has 10 000 columns (temporal dimension - $5\text{ s} \times 2000\text{ Hz}$) and 12 rows (12 electrode channels). Therefore, the dimensions of X are $(12 \times 10\,000)$. We normalize the data along the time dimension for every channel. We construct a sample covariance SPD matrix $P = \frac{1}{10000}XX^T$. P has dimensions (12×12) . Therefore, the SPD matrices are represented in \mathcal{S}_{12}^+ (space of SPD matrices whose dimensions are 12×12). We use MDM, SVM, and k -medoids algorithms as explained previously to classify the SPD matrices in \mathcal{S}_{12}^+ . We compare the results obtained with our methods to results obtained in Sun *et al* [23] and Rahimian *et al* [20] (table 1). We provide the results for all 40 subjects using manifold methods in table 2.

Classification

Table 1. Our proposed methods perform better by leveraging manifold representation. The proposed unsupervised k -medoids algorithm, to the best of our knowledge, is the only unsupervised algorithm for sEMG signal classification. Unlike other methods which have neural networks with tens of thousands of parameters, our algorithms are computationally efficient.

	Method	Accuracy
Sun <i>et al</i> [23]	4-layer 3rd order dilation	0.824
	4-layer 3rd order dilation (pure LSTM)	0.797
	4-layer 2nd order dilation (pure LSTM)	0.796
	4-layer 1st order dilation (pure LSTM)	0.793
	4-layer baseline	0.753
	2-layer CNN	0.746
	2-layer LSTM	0.702
	1-layer LSTM	0.684
	2-layer MLP	0.662
Rahimian <i>et al</i> [20]	SVM (Euclidean)	0.307
	TEMGNet 200 ms window	0.821
	TEMGNet 300 ms window	0.829
Proposed manifold methods	Manifold MDM	0.92
	Manifold SVM	0.93
	Manifold k -medoids	0.82

Table 2. Classification accuracy for 40 subjects in *Dataset 1*. Following the works in Sun *et al* [23] and Rahimian *et al* [20], for each gesture, we use repetitions 1, 3, 4, and 6 for training and repetitions 2 and 5 for testing of MDM and SVM algorithms.

Subject number	Classification methods		
	MDM	SVM ($\gamma = 8$)	k -medoids
0	1.0	1.0	0.90
1	0.94	0.97	0.86
2	0.97	0.97	0.78
3	0.94	0.94	0.79
4	0.97	1.0	0.85
5	0.85	0.85	0.79
6	0.88	0.88	0.69
7	0.85	0.91	0.80
8	0.97	1.0	0.85
9	0.88	0.91	0.87
10	0.97	0.91	0.84
11	0.85	0.91	0.79
12	0.97	0.94	0.89
13	1.0	0.97	0.93
14	0.91	0.97	0.81
15	0.91	0.88	0.66
16	0.97	0.97	0.78
17	0.88	0.91	0.83
18	0.91	0.97	0.85
19	0.88	0.88	0.83
20	0.88	0.94	0.84
21	0.91	0.91	0.85
22	0.88	0.88	0.83
23	0.91	0.94	0.78
24	0.91	0.94	0.84
25	0.97	0.97	0.85
26	0.97	0.94	0.87
27	0.91	0.94	0.87
28	0.91	0.88	0.75
29	0.82	0.91	0.76
30	0.88	0.88	0.68
31	0.91	0.88	0.84
32	0.94	0.97	0.85
33	0.76	0.82	0.73
34	0.97	0.97	0.84
35	0.97	0.88	0.80
36	0.94	1.0	0.89
37	0.97	0.97	0.96
38	0.97	0.94	0.84
39	0.97	0.97	0.86
Average	0.92	0.93	0.82

4.2. Dataset 2

4.2.1. Preprocessing

In *Dataset 2*, sEMG data was collected at a frequency of 2048 Hz using 128 electrodes. The duration of each gesture varied and we denote it using a variable \mathcal{T} . The data corpus consisted of 65 unique hand gestures with each gesture repeated five times. For a detailed description, refer to Malešević *et al* [17]. For each gesture, sEMG data is a matrix X which has \mathcal{T} columns (temporal dimension) and 128 rows (128 electrode channels). Therefore, the dimensions of X are $(128 \times \mathcal{T})$. We normalize the data along the time dimension for every channel. We construct a sample covariance

SPD matrix $P = \frac{0.9}{\mathcal{T}}XX^T + \frac{0.1}{128}\text{trace}(\frac{1}{\mathcal{T}}XX^T)\mathcal{I}_{128 \times 128}$ (see appendix C for why we add a shrinkage estimator here), where $\mathcal{I}_{128 \times 128}$ is a identity matrix of dimensions (128×128) . P has dimensions (128×128) . Therefore, the SPD matrices are represented in \mathcal{S}_{128}^+ . We use MDM, SVM, and k -medoids algorithms as explained previously to classify the SPD matrices in \mathcal{S}_{128}^+ and present the results using manifold methods in table 3. We compare the results with methods in Montazerin *et al* [18] in table 4.

Classification

Table 3. Classification accuracy averaged across 19 subjects in *Dataset 2*. Following the work in Montazerin *et al* [18], we perform five-fold cross validation analysis.

Fold number	Classification methods		
	MDM	SVM ($\gamma = 0.1$)	k -medoids
1	0.83 \pm 0.07	0.84 \pm 0.08	0.87 \pm 0.05
2	0.95 \pm 0.04	0.96 \pm 0.03	
3	0.96 \pm 0.03	0.97 \pm 0.03	
4	0.95 \pm 0.04	0.96 \pm 0.04	
5	0.91 \pm 0.05	0.92 \pm 0.04	
Average	0.92 \pm 0.07	0.93 \pm 0.07	0.87 \pm 0.05

Table 4. The performance of the proposed methods match the performance of the transformer method in Montazerin *et al* while being computationally efficient. Moreover, the proposed methods are better suited for deployment across individuals and real-time adaptation due to the transparent nature of the algorithms. For example, drift in sEMG signals due to change in sensor position or muscle fatigue can be captured simply by updating the centroids of the SPD matrices of the manifold MDM algorithm, rather than having to finetune or retrain a transformer repeatedly.

	Method	Accuracy
Montazerin <i>et al</i> [18]	512 sample window and 128 channels (their best)	0.92
	Manifold MDM	0.92
Proposed manifold methods	Manifold SVM	0.93
	Manifold k -medoids	0.87

4.3. Dataset 3

4.3.1. Preprocessing

In *Dataset 3*, sEMG data was collected at a frequency of 2000 Hz using 12 electrodes. Each gesture was 2 s long followed by a 2 s long resting position. For each gesture, sEMG data is a matrix X which has 4000 columns (temporal dimension – 2 s \times 2000 Hz) and 12 rows (12 electrode channels). Therefore, the dimensions of X are (12×4000) . We normalize the data along the time dimension for every channel. We construct a sample covariance SPD matrix $P = \frac{1}{4000}XX^T$. P has dimensions (12×12) . Therefore, the SPD matrices are represented in \mathcal{S}_{12}^+ . We use MDM,

SVM and k -medoids algorithms as explained previously to classify the SPD matrices in \mathcal{S}_{12}^+ and present the results in table 5.

Classification

Table 5. Classification accuracy for 30 subjects in *Dataset 3*. Data from the first 3 sessions are used for training (that is, the first 18 repetitions) and data from the last 3 sessions (that is, the last 18 repetitions) are used for testing of MDM and SVM algorithms.

Subject number	Classification methods		
	MDM	SVM ($\gamma = 1$)	k -medoids
0	0.97	0.99	0.94
1	0.61	0.69	0.48
2	0.62	0.76	0.61
3	0.76	0.83	0.60
4	0.92	0.93	0.74
5	0.82	0.86	0.63
6	0.94	0.97	0.88
7	0.94	0.95	0.74
8	0.97	0.97	0.93
9	0.92	0.94	0.74
10	0.84	0.86	0.62
11	0.79	0.81	0.62
12	0.95	0.97	0.93
13	0.84	0.84	0.73
14	0.82	0.84	0.64
15	0.57	0.66	0.50
16	0.92	0.93	0.76
17	0.85	0.89	0.85
18	0.53	0.57	0.35
19	0.82	0.84	0.61
20	0.83	0.87	0.72
21	0.82	0.89	0.72
22	0.93	0.94	0.70
23	0.88	0.92	0.91
24	0.55	0.55	0.26
25	0.78	0.82	0.55
26	0.83	0.89	0.83
27	0.78	0.86	0.68
28	0.99	1.0	0.99
29	0.89	0.91	0.72
Average	0.82	0.86	0.70

5. Data visualization

We use t -distributed stochastic neighbor embedding (t -SNE) [24] to visualize the SPD covariance matrices of hand gestures by replacing the Euclidean distance in t -SNE with Riemannian geodesic distance. t -SNE embedding reveals that the SPD matrices from different subjects lie in different neighborhoods of the manifold as shown in figure 3. This difference in sEMG signals is due to the combined influence of various anatomical, physiological, and circumstantial factors and is reflected in a single geodesic distance metric across all individuals as shown in figure 4. Due to this difference in spatial muscle contraction

patterns across individuals, it is difficult to generalize deep learning algorithms throughout the population. Nevertheless, with this appropriate non-Euclidean representation of the data, spatial muscle contraction patterns within an individual are distinct enough to distinguish different gestures in an unsupervised manner as shown in figures 5 and 9. That is, the Riemannian representation obviates the need for complex transfer learning paradigms and retraining of models while deploying across individuals. Note that since patterns from different individuals occupy separate neighborhoods on the manifold, directly comparing gestures across all subjects results in extremely poor gesture differentiation (figure 6). However, using parallel transport, these distinct gesture patterns can be aligned across individuals with an accuracy bounded by the accuracy of unsupervised classification (figure 7). Figure 8 shows why *parallel* transport, as opposed to Euclidean transport, is appropriate in the manifold space.

6. Discussion

One of the main challenges to widespread adoption of upper limb sEMG decoding is the inevitable signal variability across individuals (due to numerous anatomical and physiological differences) and across contexts or sessions (e.g. changes in electrode location). Here we leverage the observation that complex interactions of MU activation generating sEMG signals give rise to manifold-valued data. Specifically, we empirically demonstrate that covariance matrices corresponding to different gestures naturally cluster separately on a Riemannian manifold. Not only does manifold-space analysis provide a natural and low-dimensional classification, it also enables a transparent and analytically well-defined means of adapting to signal variability across individuals and contexts. This ability is particularly relevant in biosignal/neural interfaces, which are intimate by design and thus have high barriers to collecting data at scale (unlike text, image, and video scraped from internet). This limitation recommends sEMG decoding paradigms that not only can rapidly adapt across individuals but also can be built and updated with very little data. Our proposed methods, by leveraging the topological structure of the data, do precisely that.

An alternate approach to sEMG decoding uses neural networks on the native (Euclidean) sEMG representations. However in contrast to manifold-space analysis, convolutional and recurrent networks (in Euclidean space) require large models and extensive training datasets from many individuals, from dozens [3] to thousands [13] for transfer learning. Furthermore, [13] demonstrates that neural architectures follow an inverse power law for both model parameters and data quantity. That is, to decrease classification error in models that generalize across individuals, one must continue to increase

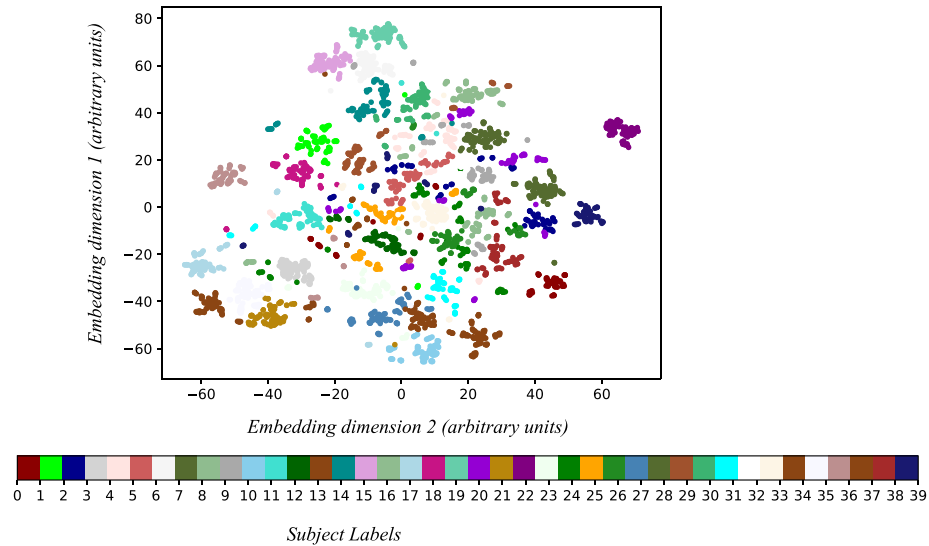


Figure 3. *t*-SNE of SPD covariance matrices using Riemannian distance indicates that the SPD matrices from different subjects lie in different neighborhoods of the manifold. This is due to shift in sEMG signals owing to the combined effect of various anatomical, physiological, and circumstantial factors. Embedding is for *Dataset 1*. Embedding is colored according to subjects. Each of the 40 subjects performed 102 trials (17 gestures, each repeated 6 times).

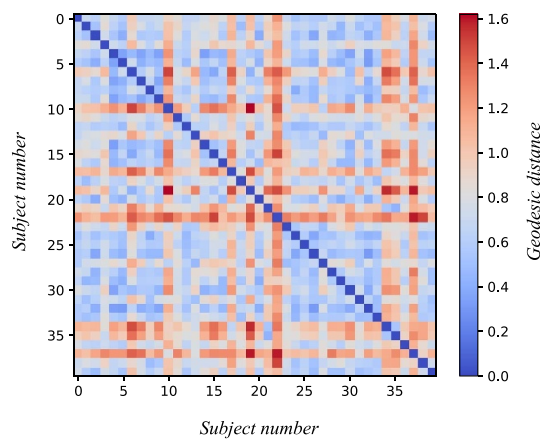


Figure 4. Riemannian geodesic distance between the centroids of SPD covariance matrices of 40 subjects in *Dataset 1*. Geodesic distance quantifies the differences in sEMG signals between subjects due to the combined effect of various physiological and anatomical factors. The centroid of a given subject is calculated as the *Log-Cholesky* average of SPD covariance matrices of all 102 trials (17 gestures, each repeated 6 times). *X* and *Y* axes are numbered according to subjects.

both data quantity and model size: the broader the generalization, the more data and parameters are required. This is due to the fact that these neural networks assume inherent Euclidean data structure, which sEMG signals lack, and therefore must attain generalizability through extensive training. The same report [13] also discusses the differences in sEMG signals across individuals. After evaluating the data from several participants, no clear clusters of participants with distinct performance statistics were evident, which makes it challenging to explain and quantify the inter-individual differences and their relationship to raw signals. Our results corroborate these observations but also provide an explanation that quantifies these differences and explicitly represents the idiosyncratic

relationship between individuals and their sEMG signals (see figure 3). Additionally, our approach complements and extends prior work by explaining how to align sEMG signals across individuals (see figures 6 and 7).

Finally, the proposed methods are well suited for real-time adaptation. For example, one can devise methods to update centroids to track changes in sensor positions (as the wrist band shifts or slips), signal drift from muscles due to strain and fatigue, or decoding biases, as when users subtly change how they perform a given gesture. As a consequence of operating in manifold space, our approach promises to overcome these numerous practical, everyday impediments to sEMG decoding in real-world applications.

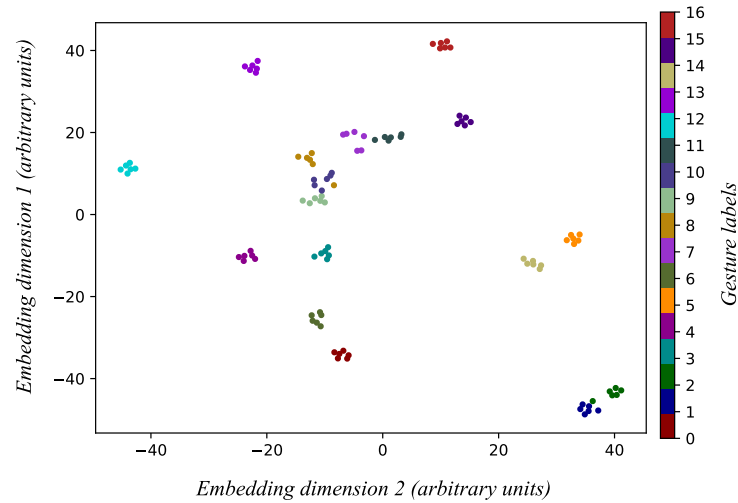


Figure 5. *t*-SNE of SPD matrices of *Subject 0* from *Dataset 1* shows that different gestures within a subject have contrasting spatial patterns. We can classify these distinct gestures with supervised algorithms such as minimum distance to mean (MDM) and support vector machine (SVM) or unsupervised algorithms such as *k*-medoids clustering using Riemannian distance. Classification accuracy using the above methods is presented in table 2 for all 40 subjects. Embedding is colored according to gestures. The subject performed 17 gestures with each gesture repeated six times. The gestures are: 0: thumb up, 1: extension of index and middle—flexion of the others, 2: flexion of ring and little finger—extension of the others, 3: thumb opposing base of little finger, 4: abduction of all fingers, 5: fingers flexed together in fist, 6: pointing index, 7: adduction of extended fingers, 8: wrist supination (axis: middle finger), 9: wrist pronation (axis: middle finger), 10: wrist supination (axis: little finger), 11: wrist pronation (axis: little finger), 12: wrist flexion, 13: wrist extension, 14: wrist radial deviation, 15: wrist ulnar deviation, and 16: wrist extension with closed hand.

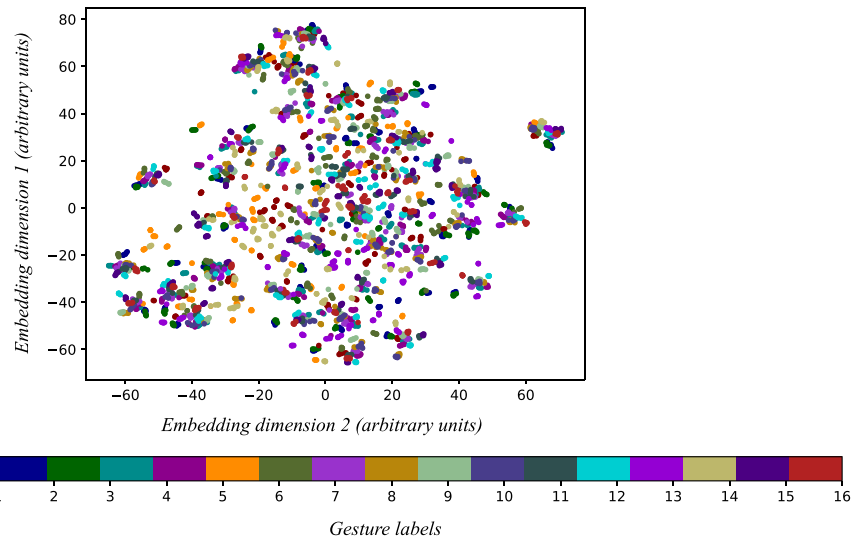


Figure 6. *t*-SNE of SPD covariance matrices using Riemannian distance without accounting for intersubject differences reveals that the SPD matrices for the same gesture from different subjects do not cluster together. This is the same embedding in figure 3 colored according to gestures (instead of subjects). Each of the 40 subjects performed 102 trials (17 gestures, each repeated 6 times). The gestures are: 0: thumb up, 1: extension of index and middle—flexion of the others, 2: flexion of ring and little finger—extension of the others, 3: thumb opposing base of little finger, 4: abduction of all fingers, 5: fingers flexed together in fist, 6: pointing index, 7: adduction of extended fingers, 8: wrist supination (axis: middle finger), 9: wrist pronation (axis: middle finger), 10: wrist supination (axis: little finger), 11: wrist pronation (axis: little finger), 12: wrist flexion, 13: wrist extension, 14: wrist radial deviation, 15: wrist ulnar deviation, and 16: wrist extension with closed hand.

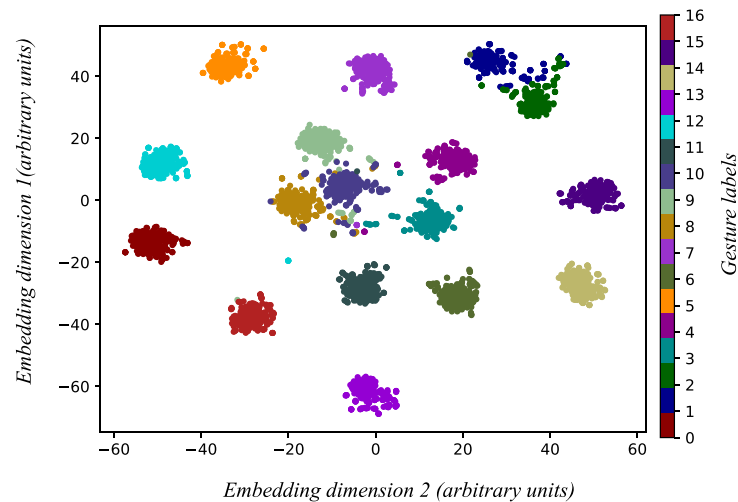


Figure 7. *t*-SNE of SPD covariance matrices using Riemannian distance after aligning the gestures using *parallel transport* as described in appendix B and illustrated in figure 8. Data is aligned assuming ground truth labels for visualization purposes. Otherwise, alignment accuracy is bounded by the accuracy of unsupervised classification. This demonstrates how data from different individuals in figure 6 can be aligned according to gestures so that the same gestures from different individuals are transported to the same neighborhood in the manifold space. Embedding is colored according to gestures. Each of the 40 subjects performed 102 trials (17 gestures, each repeated 6 times). The gestures are: 0: thumb up, 1: extension of index and middle—flexion of the others, 2: flexion of ring and little finger—extension of the others, 3: thumb opposing base of little finger, 4: abduction of all fingers, 5: fingers flexed together in fist, 6: pointing index, 7: adduction of extended fingers, 8: wrist supination (axis: middle finger), 9: wrist pronation (axis: middle finger), 10: wrist supination (axis: little finger), 11: wrist pronation (axis: little finger), 12: wrist flexion, 13: wrist extension, 14: wrist radial deviation, 15: wrist ulnar deviation, and 16: wrist extension with closed hand.

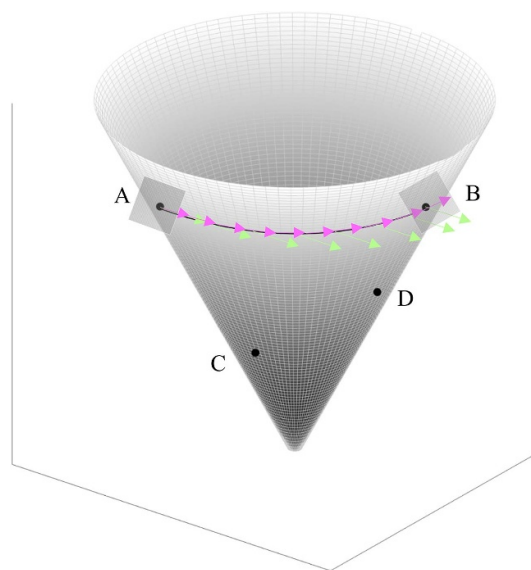


Figure 8. Euclidean transport is inappropriate in the manifold space. Point A is an SPD matrix that represents the channel covariance for a given gesture, say a pinch, for a given subject. Point B is another SPD matrix representing the reference location for that gesture on the manifold: say, a particular reference subject's centroid for the pinch gesture. The length of the curve joining A and B is the geodesic distance between the two points. Points C and D, like A and B are SPD matrices that represent different gestures; for instance, the reference locations for a power grasp and a wrist flexion. *Green* arrows illustrate the Euclidean transport of a tangent vector from A to B. *Pink* arrows represent the *parallel transport* of a tangent vector from A to B. Parallel transport rotates the vector along the path from A to B so that the vector in the tangent plane of A remains in the tangent plane of B when transported. It can be seen that the Euclidean transport of a vector in the tangent plane of A results in vectors that are no longer in the tangent plane along the path to B. The Euclidean transport of vectors therefore cannot appropriately traverse a geodesic. The *square patches* at A and B represent the tangent planes.

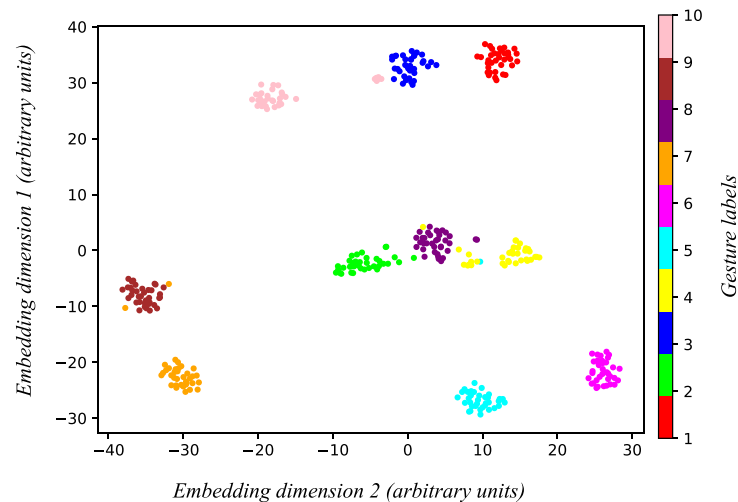


Figure 9. *t*-SNE of SPD matrices of *Subject 0* from *Dataset 3* shows that different gestures within a subject have contrasting spatial patterns. We can classify these distinct gestures with supervised algorithms such as minimum distance to mean (MDM) and support vector machine (SVM) or unsupervised algorithms such as *k*-medoids clustering using Riemannian distance. Classification accuracy using the above methods is presented in table 5 for all 30 subjects. Embedding is colored according to gestures. The subject performed 10 gestures with each gesture repeated 36 times. Ten gestures are: 1 - Down, 2 - Index finger pinch, 3 - Left, 4 - Middle finger pinch, 5 - Index point, 6 - Power grasp, 7 - Right, 8 - Two finger pinch, 9 - Up, 10 - Splay.

7. Limitations

Our analysis and experiments are restricted to discrete gesture tasks only. There is a need to expand these methods for continuous tasks (such as handwriting decoding). Additionally, the methods need to be tested in real-world and real-time scenarios. As the SPD matrices are based on (bivariate) covariance matrices, it remains to be seen how much more information about gestures may be better represented in individual channels rather than by their relationships, or by higher order statistics among two or more channels.

Data availability statement

Ninapro DB-2 dataset is publicly available through the following link: <https://ninapro.hevs.ch/> [2].

High density sEMG dataset is publicly available through the following link: <https://doi.org/10.6084/m9.figshare.c.5090861> [17]. UCD-MyoVerse-Hand-0 dataset is publicly available through the following link: DOI:10.17605/OSF.IO/ZCR43.

Codes are available on GitHub: <https://github.com/HarshavardhanaTG/GeometryOFsEMG>. The data that support the findings of this study are openly available at the following URL/DOI: <https://www.doi.org/10.17605/OSF.IO/ZCR43>.

Acknowledgments

This work was supported by Meta Platforms Technologies (Facebook Research) with an award to L M M through the Ethical Neurotechnology program and by the UC Davis School of Medicine Cultivating Team Science Award to L M M. We would like to

thank Stephanie Naufel at Facebook Reality Labs for her valuable guidance. We thank Carlos Carrasco, Marcus Battraw, and Jonathon Schofield for their advice in designing the experiment and collection of data. We also thank Neha Kaul, Safa Amar, and Saniya Kotwal for their help in collection of data.

Ethical statement

Research was conducted in accordance with the principles embodied in the Declaration of Helsinki and in accordance with the University of California, Davis Institutional Review Board Administration protocol 2078695-1. All participants provided written informed consent. Consent was also given for publication of the deidentified data by all participants. Participants were healthy volunteers and were selected from any gender and all ethnic and racial groups. Subjects were aged 18 or above, were able to fully understand spoken and written English, and were capable of following task instructions. Subjects had no skin conditions or wounds where electrodes were placed. Subjects were excluded if they had uncorrected vision problems or neuromotor disorders that prevented them from making hand gestures. Children, adults who were unable to consent, and prisoners were not included in the experiments.

Author contributions

L M M conceptualized the study and framed the problem statements. H T G formulated the mathematical framework, implemented the codes, and collected the data. H T G and L M M authored and reviewed the manuscript.

Conflict of interest

The authors declare no competing interests.

Appendix A. Manifold SVM kernel

We shall prove that the kernel $\mathcal{K} = \exp(-\gamma d_{\mathcal{L}_c^+}^2(L_1, L_2))$ for $L_1, L_2 \in \mathcal{L}_c^+$ is a valid kernel for all $\gamma > 0$. For a kernel to be valid, it must be positive definite [10].

From theorem 5.2 in Jayasumana *et al* [10], a kernel $\mathcal{K} : \mathcal{L}_c^+ \times \mathcal{L}_c^+ \rightarrow \mathbb{R} := \exp(-\gamma d_{\mathcal{L}_c^+}^2(L_1, L_2))$ is positive definite for all $\gamma > 0$ if and only if $d_{\mathcal{L}_c^+}^2(L_1, L_2)$ is negative definite.

From lemma 5.5 in Jayasumana *et al* [10], if $\psi : \mathcal{L}_c^+ \rightarrow F$ (F is the Frobenius inner product space) is a function, then, $\mathcal{O} : \mathcal{L}_c^+ \times \mathcal{L}_c^+ \rightarrow \mathbb{R}$ defined by $\mathcal{O}(L_1, L_2) = \|\psi(L_1) - \psi(L_2)\|_F^2$ is negative definite.

Following theorem 6.1 [10], $\mathcal{K} : \mathcal{L}_c^+ \times \mathcal{L}_c^+ \rightarrow \mathbb{R}$ given by $\mathcal{K}(L_1, L_2) = \exp(-\gamma d_{\mathcal{L}_c^+}^2(L_1, L_2))$ is a positive definite kernel for all $\gamma > 0$ if and only if there exists a function $\psi : \mathcal{L}_c^+ \rightarrow F$ such that $d_{\mathcal{L}_c^+}^2(L_1, L_2) = \|\psi(L_1) - \psi(L_2)\|_F^2$.

We can now define $\psi = \lfloor L \rfloor + \log \mathbb{D}(L)$ for $L \in \mathcal{L}_c^+$. We have $d_{\mathcal{L}_c^+}^2(L_1, L_2) = \{\|\lfloor L_1 \rfloor - \lfloor L_2 \rfloor\|_F^2 + \|\log \mathbb{D}(L_1) - \log \mathbb{D}(L_2)\|_F^2\}^{1/2}$. $\|\psi(L_1) - \psi(L_2)\|_F = \|\lfloor L_1 \rfloor + \log \mathbb{D}(L_1) - \lfloor L_2 \rfloor - \log \mathbb{D}(L_2)\|_F = \{\|\lfloor L_1 \rfloor - \lfloor L_2 \rfloor\|_F^2 + \|\log \mathbb{D}(L_1) - \log \mathbb{D}(L_2)\|_F^2\}^{1/2}$. Therefore, $d_{\mathcal{L}_c^+}^2(L_1, L_2) = \|\psi(L_1) - \psi(L_2)\|_F^2$. Hence, the kernel $\mathcal{K} = \exp(-\gamma d_{\mathcal{L}_c^+}^2(L_1, L_2))$ is a valid kernel.

Appendix B. Parallel transport

As given in Lin [15], the logarithm map from the manifold to its tangent space at L is given by

$$\widetilde{\text{Log}}_L K = \lfloor K \rfloor - \lfloor L \rfloor + \mathbb{D}(L) \log \left\{ \mathbb{D}(L)^{-1} \mathbb{D}(K) \right\}, \quad (.1)$$

where $L, K \in \mathcal{L}_c^+$ and $\widetilde{\text{Log}}_L K \in T_L \mathcal{L}_c^+$.

The exponential map from the tangent space to the manifold space is given by,

$$\widetilde{\text{Exp}}_L X = \lfloor L \rfloor + \lfloor X \rfloor + \mathbb{D}(L) \exp \left\{ \mathbb{D}(X) \mathbb{D}(L)^{-1} \right\}, \quad (.2)$$

where $L \in \mathcal{L}_c^+$, $X \in T_L \mathcal{L}_c^+$, and $\widetilde{\text{Exp}}_L X \in \mathcal{L}_c^+$.

A tangent vector $X \in T_L \mathcal{L}_c^+$ is parallelly transported to the tangent vector

$$\lfloor X \rfloor + \mathbb{D}(K) \mathbb{D}(L)^{-1} \mathbb{D}(X) \quad (.3)$$

at K [15].

Given a set of subjects s and a set of gestures g , let us denote a set of gestures (Cholesky factorized covariance SPD matrices) belonging to a particular subject as \mathcal{G}_s^g . Parallel transport in figure 7 is achieved using the algorithm below.

For visualization purposes, we performed parallel transport assuming ground truth labels. Otherwise, the accuracy of parallel transport is bounded by the accuracy of an unsupervised classifier. Algorithm 1 demonstrates a method to align multivariate sEMG timeseries from different individuals to the same neighborhood in the manifold space.

Algorithm 1 Parallel transport


Input : Cholesky matrices \mathcal{G}_s^g **Output :** Parallely transported Cholesky matrices.


- (1) Calculate Riemannian mean $\bar{\mathcal{G}}_s^g = \mathbb{E}(\text{all elements in } \mathcal{G}_s^g)$ using equation (4).
 - (2) Map all elements in \mathcal{G}_s^g to the tangent space at $\bar{\mathcal{G}}_s^g$ using equation (1). Let us denote this mapped set as $T_{\bar{\mathcal{G}}_s^g} \mathcal{G}_s^g$.
 - (3) Parallely transport the tangent vectors in $T_{\bar{\mathcal{G}}_s^g} \mathcal{G}_s^g$ to the tangent space at $\bar{\mathcal{G}}_{s=\text{Reference}}^g$. We chose *Subject 0* as our reference.
 - (4) Map all the parallely transported vectors in the tangent space of $\bar{\mathcal{G}}_{s=\text{Reference}}^g$ to the manifold space using equation (2).
-

Appendix C. Shrinkage estimator

A covariance matrix P is a positive semi-definite matrix (for every non-zero real column vector z , $z^T P z \geq 0$. P has real entries only). To make $z^T P z > 0$ (to make a positive semi-definite matrix into to positive definite matrix), we add a shrinkage estimator. Specifically, for a matrix $X_{128 \times \tau}$, we computed the corresponding SPD matrix as $P = \frac{0.9}{\tau} X X^T + \frac{0.1}{128} \text{trace}(\frac{1}{\tau} X X^T) \mathcal{I}_{128 \times 128}$. This insight stems from the fact that covariance matrix should be diagonally dominant for it to be a SPD matrix and by adding a positive diagonal matrix, we are ensuring the same. Refer to [14], [27] for more details.

ORCID iDs

Harshavardhana T Gowda  <https://orcid.org/0009-0009-0552-7737>

Lee M Miller  <https://orcid.org/0000-0001-5094-6724>

References

- [1] Arsigny V, Fillard P, Pennec X and Ayache N 2007 Geometric means in a novel vector space structure on symmetric positive-definite matrices *SIAM J. Matrix Anal. Appl.* **29** 328–47
- [2] Atzori M, Gijsberts A, Castellini C, Caputo B, Mittaz Hager A-G, Elsig S, Giatsidis G, Bassetto F and Müller H 2014 Electromyography data for non-invasive naturally-controlled robotic hand prostheses *Sci. Data* **1** 1–13
- [3] Côté-Allard U, Latyr Fall C, Drouin A, Campeau-Lecours A, Gosselin C, Glette K, Laviolette F and Gosselin B 2019 Deep learning for electromyographic hand gesture signal classification using transfer learning *IEEE Trans. Neural Syst. Rehabil. Eng.* **27** 760–71
- [4] Enoka R M and Duchateau J 2008 Muscle fatigue: what, why and how it influences muscle function *J. Physiol.* **586** 11–23
- [5] Farina D, Merletti R and Enoka R M 2004 The extraction of neural strategies from the surface EMG *J. Appl. Physiol.* **96** 1486–95
- [6] Geng W, Du Y, Jin W, Wei W, Hu Y and Li J 2016 Gesture recognition by instantaneous surface EMG images *Sci. Rep.* **6** 36571
- [7] Hu Y, Wong Y, Wei W, Du Y, Kankanhalli M and Geng W 2018 A novel attention-based hybrid CNN-RNN architecture for sEMG-based gesture recognition *PLoS One* **13** e0206049
- [8] Hudgins B, Parker P and Scott R N 1993 A new strategy for multifunction myoelectric control *IEEE Trans. Biomed. Eng.* **40** 82–94
- [9] Huebner A, Faenger B, Schenk P, Scholle H-C and Anders C 2015 Alteration of surface EMG amplitude levels of five major trunk muscles by defined electrode location displacement *J. Electromyogr. Kinesiol.* **25** 214–23
- [10] Jayasumana S, Hartley R, Salzmann M, Li H and Harandi M 2015 Kernel methods on Riemannian manifolds with Gaussian RBF kernels *IEEE Trans. Pattern Anal. Mach. Intell.* **37** 2464–77
- [11] Khushaba R N, Al-Timemy A H, Williams Samuel O and Scheme E J 2022 Myoelectric control with fixed convolution-based time-domain feature extraction: exploring the spatio-temporal interaction *IEEE Trans. Hum. Mach. Syst.* **52** 1247–57
- [12] Kleine B U, Stegeman D F, Mund D and Anders C 2001 Influence of motoneuron firing synchronization on sEMG characteristics in dependence of electrode position *J. Appl. Physiol.* **91** 1588–99
- [13] Ctrl labs at Reality Labs Sussillo D, Kaifosh P and Reardon T 2024 A generic noninvasive neuromotor interface for human-computer interaction *bioRxiv Preprint* <https://doi.org/10.1101/2024.02.23.581779>
- [14] Ledoit O and Wolf M 2004 A well-conditioned estimator for large-dimensional covariance matrices *J. Multivariate Anal.* **88** 365–411
- [15] Lin Z 2019 Riemannian geometry of symmetric positive definite matrices via Cholesky decomposition *SIAM J. Matrix Anal. Appl.* **40** 1353–70
- [16] Lucas M-F, Gaufriau A, Pascual S, Doncarli C and Farina D 2008 Multi-channel surface EMG classification using support vector machines and signal-based wavelet optimization *Biomed. Signal Process. Control* **3** 169–74
- [17] Malešević N, Olsson A, Sager P, Andersson E, Cipriani C, Controzzi M, Björkman A and Antfolk C 2021 A database of high-density surface electromyogram signals comprising 65 isometric hand gestures *Sci. Data* **8** 63
- [18] Montazerin M, Rahimian E, Naderkhani F, Atashzar S F, Yanushkevich S and Mohammadi A 2023 Transformer-based hand gesture recognition from instantaneous to fused neural decomposition of high-density EMG signals *Sci. Rep.* **13** 11000
- [19] Quivira F, Koike-Akino T, Wang Y and Erdogmus D 2018 Translating sEMG signals to continuous hand poses using recurrent neural networks *2018 IEEE EMBS Int. Conf. on Biomedical & Health Informatics (BHI)* pp 166–9
- [20] Rahimian E, Zabihi S, Asif A, Farina D, Atashzar S F and Mohammadi A 2021 TEMGNet: deep transformer-based decoding of upperlimb sEMG for hand gestures recognition (arXiv:2109.12379)
- [21] Rahimian E, Zabihi S, Farokh Atashzar S, Asif A and Mohammadi A 2020 Surface EMG-based hand gesture recognition via hybrid and dilated deep neural network architectures for neurorobotic prostheses *J. Med. Robot. Res.* **5** 2041001
- [22] Rahimian E, Zabihi S, Farokh Atashzar S, Asif A and Mohammadi A 2020 XceptionTime: independent time-window XceptionTime architecture for hand gesture classification *ICASSP 2020 - 2020 IEEE Int. Conf. on Acoustics, Speech and Signal Processing (ICASSP)* pp 1304–8
- [23] Sun T, Hu Q, Gulati P and Farokh Atashzar S 2021 Temporal dilation of deep LSTM for agile decoding of sEMG: application in prediction of upper-limb motor intention in neurorobotics *IEEE Robot. Autom. Lett.* **6** 6212–9

- [24] van der Maaten L and Hinton G 2008 Visualizing data using t-SNE *J. Mach. Learn. Res.* **9** 2579–605 (available at: <http://jmlr.org/papers/v9/vandermaaten08a.html>)
- [25] Wei W, Wong Y, Du Y, Hu Y, Kankanhalli M and Geng W 2019 A multi-stream convolutional neural network for sEMG-based gesture recognition in muscle-computer interface *Pattern Recognit. Lett.* **119** 131–8
- [26] Xiong D, Zhang D, Zhao X, Chu Y and Zhao Y 2022 Learning non-euclidean representations with SPD manifold for myoelectric pattern recognition *IEEE Trans. Neural Syst. Rehabil. Eng.* **30** 1514–24
- [27] Ying J, Wei Q and Zhou X 2022 Riemannian geometry-based transfer learning for reducing training time in c-VEP BCIs *Sci. Rep.* **12** 9818
- [28] Zardoshti-Kermani M, Wheeler B C, Badie K and Hashemi R M 1995 EMG feature evaluation for movement control of upper extremity prostheses *IEEE Trans. Rehabil. Eng.* **3** 324–33